



Atom-triggered epitaxial growth of Bi-based perovskite heterojunctions for promoting interfacial charge transfer

Yuan Teng^{a,b,1}, Jing-Hua Chen^{a,1}, Yu-Hua Huang^a, Zi-Chun Zhou^a, Xu-Dong Wang^a, Dai-Bin Kuang^{a,*}, Hong-Yan Chen^{a,*}

^a MOE Key Laboratory of Bioinorganic and Synthetic Chemistry, Lehn Institute of Functional Materials, School of Chemistry, Sun Yat-sen University, Guangzhou 510006, PR China

^b National Experimental Teaching Demonstration Center for Chemistry, College of Chemistry and Chemical Engineering, Jishou University, Jishou 416000, PR China

ARTICLE INFO

Keywords:

Atom-triggered
Epitaxial growth
Bi-based perovskite
In situ Z-scheme heterojunction
Photocatalysis

ABSTRACT

The construction of high-quality heterojunction with staggered band structure and close-contact interface, to satisfy both the thermodynamic and dynamic prerequisites of charge transfer, is the key to improve the charge separation of halide perovskites. The *in situ* growth of perovskite heterojunction via cosharing atoms provides an appealing solution to tackle this dilemma, but it remains a big challenge owing to the lack of appropriate precursors. Here, we design a novel visible-light responsive $\text{Co}_x\text{Bi}_{2-x}\text{O}_2\text{CO}_3$ nanosheet, and use it as self-template to epitaxially grow $\text{Cs}_3\text{Bi}_2\text{Br}_9$ nanosheet. It is revealed that close-contact 2D/2D heterointerfaces with strong chemical and electronic coupling are built via Bi atom bridge. Moreover, incorporating Co^{3+} into $\text{Bi}_2\text{O}_2\text{CO}_3$ plays critical roles in heterojunction growth by regulating both the electronic structure and growth dynamics of $\text{Cs}_3\text{Bi}_2\text{Br}_9$. Triggered by the effect of Co and the matched Bi lattice with $\text{Cs}_3\text{Bi}_2\text{Br}_9$, the $\text{Co}_x\text{Bi}_{2-x}\text{O}_2\text{CO}_3/\text{Cs}_3\text{Bi}_2\text{Br}_9$ heterojunction can drive the fast Z-scheme transfer and separation of photoexcited charge carriers.

1. Introduction

In recent years, lead halide perovskites (HPVK), have triggered substantial interests in photoelectric applications including solar cells, light-emitting diodes, photodetectors and photocatalysis due to their high tolerance of defects, excellent optoelectrical properties and ease of synthesis [1–4]. In view of the lead toxicity, much efforts have been devoted to developing eco-friendly halide perovskites by substituting Pb^{2+} with other metal cations, such as Bi^{3+} , Sb^{3+} or Cu^{2+} , etc., which always show better environmental stability [5–11]. However, replacing Pb^{2+} by Bi^{3+} usually leads to low dimensional crystal structure, e.g., 2D, 1D or 0D structure. In addition, vacancies and deep trapping states are liable to form, leading to low carrier mobility and severe carrier recombination [12–14]. Therefore, it is of great significance to enhance the photogenerated-charge separation efficiency of Bi-based perovskite materials towards their potential photoelectrical applications.

Heterojunction engineering has been widely employed to overcome the severe charge carrier recombination to improve their photon-to-electron conversion efficiency. The last five years have witnessed the

rapid development of HPVK-based heterojunction photocatalysts by incorporating HPVK with various functional materials such as graphene [15], g- C_3N_4 [16], metal oxide [17], metal sulfide [18], metal-organic frameworks [19], metal single atom [20], etc., to form type II, Z-scheme or Schottky heterojunction. In such heterostructures, staggered band structure between heterogeneous constituents is the thermodynamic prerequisite for driving the charge transfer, but the transfer speed and the corresponding charge separation efficiency largely depends on the quality of interfaces. A high-quality heterointerfaces with large contact area, low defect densities and strong interface interaction is important for fast charge transfer and separation. Therefore, different strategies including electrostatic self-assembly [21], surface modification with functional groups [22], *in situ* hydrolysis encapsulating [23, 24], etc., have been developed to engineer the interface contact of HPVK heterojunctions. However, due to the fast nucleation and growth rates of HPVK, the delicately regulation of interfacial structure and properties still remains challenging.

Recently, HPVK heterojunctions constructed via “atom-cosharing” provide a promising and appealing way to tackle this issue. In this case,

* Corresponding authors.

E-mail addresses: kuangdb@mail.sysu.edu.cn (D.-B. Kuang), chenhy33@mail.sysu.edu.cn (H.-Y. Chen).

¹ Yuan Teng and Jing-Hua Chen contributed equally to this work

the common atoms can bridge the two heterogeneous components together by serving as the nucleation sites to *in situ* grow one component on the surface of another [25–29]. Furthermore, if a low lattice mismatch ($f < 5.00\%$, f is defined as $(b-a)/a$, where a and b are the corresponding lattice spacings of the two constituents, respectively) was ensured, the interfacial defects could be suppressed largely, which would be more beneficial to the charge transfer and separation [30–32]. Embedding CsPbBr₃ nanocrystal in Cs₄PbBr₆ matrix is a typical example of atom-coshaing heterojunction in which the two constituents possess the same elements and matched crystal structure [33]. Therefore, the interfacial defects can be effectively passivated resulting in enhanced stability and photoluminescence quantum yield (PLQY) of CsPbBr₃. Another example is lead chalcogenide/perovskite heterojunction constructed *via* matched Pb sublattices [34,35], which can passivate the surface defects, improve the stability and accelerate the fast type I carrier transfer. Heteroepitaxial growth of BiOBr layers on the surface of Cs₂AgBiBr₆ wafers was also reported to passivate the defects at grain boundaries and suppressed the ionic migration effectively [36]. These results revealed that the atomic-level close contact with low defect density, strong chemical bonding and the corresponding strong electronic state interaction, could form *via* coshaing atom, which should shorten the charge transfer distance and promote the charge separation [37–40]. Inspired by the above facts, constructing high-quality type II or Z-scheme HPVK heterojunctions *via* coshaing atom should be a promising method to establish the advanced photocatalytic materials.

In 2019, we demonstrated a self-templated acid etching method to *in situ* grow Cs₂SnI₆ nanocrystals on the surface of SnS₂ nanoflower to form type II heterojunction [41]. This method is regarded as universal way to construct atom-sharing perovskite heterojunction by using metal oxide or chalcogenide semiconductors as both the functional constituent and the metal precursor of perovskites. Based on the above analysis, the challenge should move to designing appropriate functional precursors with common atom, matched band structure with perovskite, to satisfy both the thermodynamic and dynamic requirements of charge transport. With this in mind, herein, we devise a novel visible-light responsive semiconductor Co_xBi_{2-x}O₂CO₃ nanosheet and use it as self-template to *in situ* epitaxially grow Cs₃Bi₂Br₉ nanosheet *via* acid etching process. It is found that incorporating Co³⁺ to Bi₂O₂CO₃ can regulate the electronic structure of Bi₂O₂CO₃, thus ensuring matched band structure with Cs₃Bi₂Br₉. Moreover, the as-formed Co-O layer can controllably release Bi³⁺ during the acid etching, which can manipulate the growth dynamics of Cs₃Bi₂Br₉ with maintaining the structure integrity of parent nanosheet. The Bi and Co atoms trigger the epitaxial growth of Cs₃Bi₂Br₉ nanosheet on Bi₂O₂CO₃, which enables the formation of close-contact heterointerfaces with strong chemical interaction, which contributes to a strong built-in electric field to drive the rapid Z-scheme transfer and spacial separation of photoinduced charge carriers. As a proof of concept, when employing as photocatalysts for sp³ C-H activation reaction of toluene, the benzaldehyde yield rate of Co_{0.97}Bi_{1.03}O₂CO₃/Cs₃Bi₂Br₉ is 2.08-fold of that of Cs₃Bi₂Br₉ samples, for example, benzaldehyde amount of 7349.24 μmol g⁻¹ after 4 h of photocatalysis reaction, confirming the excellent charge transport and separation ability of such 2D/2D heterojunction.

2. Experimental

2.1. Materials

Hydrobromic acid (HBr, 48%), bismuth nitrate pentahydrate (Bi(NO₃)₃·5 H₂O, 99%) and absolute cesium bromide (CsBr, 99.9%) were purchased from Shanghai Aladdin Biochemical Technology Co., Ltd. 5,5-dimethyl-1-pyrroline N-oxide (DMPO) was bought from Dojindo Molecular Technologies, Inc. (Tokyo, Japan). Sodium carbonate (Na₂CO₃, A.R.) was bought from Tianjin Damao Chemical Reagent Factory. Cobalt nitrate hexahydrate (Co(NO₃)₂·6 H₂O, A.R.) and absolute toluene were purchased from Guangzhou Chemical Reagent

Factory. Sodium hydroxide (NaOH, 96%) was purchased from Guangdong Guanghua Technology Co., Ltd. The anhydrous *tert* (*t*)-butanol (99.5%) and isopropanol (99.5%) were purchased from Beijing Innochem Science & Technology Co., Ltd.

2.2. Synthesis of the Bi₂O₂CO₃ and Co_xBi_{2-x}O₂CO₃ samples

The Co_xBi_{2-x}O₂CO₃ nanosheets were synthesized by a liquid phase co-deposition synthesis method. First, 0.25 mmol Bi(NO₃)₃·5 H₂O and 0.25 mmol Co(NO₃)₂·6 H₂O were added into 70 mL deionized water under the continuous stirring and ultrasonic condition, and heated to 60 °C until all powders were completely dissolved. Then the pH value was adjusted to 10 by 1.0 M NaOH. 0.05 mmol Na₂CO₃ was added under vigorously stirring, and the mixture was heated to 80 °C with a rate of 10 °C min⁻¹ and maintained at the desired temperature for 24 h. It should be noted that the Co²⁺ was used during the synthesis process, which should undergo an oxidation reaction in hot NO₃. After cooled down to room temperature naturally, the achieved precipitates were centrifuged and washed several times with deionized water to remove impurities. Finally, the obtained products were dried at 60 °C for 24 h under vacuum condition. Similarly, the Co_xBi_{2-x}O₂CO₃ samples with the different Co content were also prepared by fixing Bi(NO₃)₃·5 H₂O at 0.25 mmol and the molar ratio of Co(NO₃)₂·6 H₂O to Bi(NO₃)₃·5 H₂O was 0.5:1, 1:1, and 2:1, respectively. For comparison, the pristine Bi₂O₂CO₃ was also synthesized by the similar synthesis route without Co (NO₃)₂·6 H₂O added.

2.3. Fabrication of the Co_xBi_{2-x}O₂CO₃/Cs₃Bi₂Br₉ hybrid and Cs₃Bi₂Br₉ samples

The heterojunction was prepared by an *in situ* acid etching strategy with Co_xBi_{2-x}O₂CO₃ as both the functional constituent and precursor of Bi³⁺. Except otherwise noted, the Co_xBi_{2-x}O₂CO₃ species involved in the heterojunction sample was Co_xBi_{2-x}O₂CO₃ (1:1), which was denoted as the Co_{0.97}Bi_{1.03}O₂CO₃ based on the ICP-AES results. Concretely, 11 mg Co_{0.97}Bi_{1.03}O₂CO₃ powders were added into 5 mL *t*-butanol and sonicated for 10 min to get a uniform dispersion solution, denoted as Solution A. And 0.60 mg CsBr was dissolved in 5 mL *t*-butanol and 50 μL HBr, denoted as Solution B. Subsequently, Solution B was drop by drop added into Solution A within 4 min and vigorously stirred for another 3 min. The as-prepared sediments were centrifuged at 10,000 rpm for 5 min, washed and dried at 60 °C in vacuum oven. The control experiments were also carried out by adjusting either the addition amount of Solution B or the dropping time. Similar procedure was used to synthesize Cs₃Bi₂Br₉ except that superfluous HBr (100 μL) was added and the reaction time was lasted to 30 min to thoroughly convert Co_{0.97}Bi_{1.03}O₂CO₃ to Cs₃Bi₂Br₉. For comparison, the physically mixed sample of Co_{0.97}Bi_{1.03}O₂CO₃ and Cs₃Bi₂Br₉ was also prepared. The Co_{0.97}Bi_{1.03}O₂CO₃ and Cs₃Bi₂Br₉ powders with the mass ratio of 3:1 were added into 5 mL isopropanol. After stirring for 3 h, the mixture was centrifuged at 10,000 rpm for 5 min and dried at 60 °C in vacuum oven, and the as-obtained sample was labelled as the Co_{0.97}Bi_{1.03}O₂CO₃ + Cs₃Bi₂Br₉. For photoelectrical tests, the suspensions of samples were centrifuged on ITO glass at 10,000 rpm for 5 min, and dried at 60 °C for 24 h to acquire the Co_{0.97}Bi_{1.03}O₂CO₃, Cs₃Bi₂Br₉, Co_{0.97}Bi_{1.03}O₂CO₃/Cs₃Bi₂Br₉, and Co_{0.97}Bi_{1.03}O₂CO₃ + Cs₃Bi₂Br₉ thin films.

2.4. Characterization and measurements

The crystal structure of materials was studied by powder X-ray diffraction (PXRD, D-MAX 2200 VPC). The Pawley refinement of the PXRD patterns obtained under capillary transmission mode was carried out to further analyze the crystal structure (SmartLab). The morphology was observed by scanning electron microscopy (SEM, Hitachi SU8010) and aberration-corrected TEM (JEOL, ARM-200 F). Light absorption properties of samples were measured by a UV-vis spectrophotometer

(Shimadzu UV-3600). Ultraviolet photoelectron spectra (UPS) and X-ray photoelectron spectroscopy (XPS) were carried out at a photoelectron spectrometer (ESCALAB Xi+, Thermo Fisher Scientific). A 405 nm laser was used as the light source to obtain the XPS spectra of samples under *in situ* illumination. The thickness of nanosheets and surface photovoltage (SPV) of samples were tested by atomic force microscope (AFM, DIMENSION FASTSCAN) and Kelvin Probe Force Microscopy (KPFM). The electron paramagnetic resonance (EPR) test was conducted on a Bruker EMXplus ESR spectrometer. DMPO was used as the radical trapper, acetonitrile/water (volume ratio of 50:1) as the solvent. The inductively coupled plasma atomic emission spectroscopy (ICP-AES) test was performed on an Optima8300. The X-ray absorption spectroscopy (XAS) including X-ray absorption near edge structure (XANES) and extended X-ray absorption fine structure (EXAFS) was performed at the Shanghai Synchrotron Radiation Facility (SSRF) (Shanghai, China).

2.5. Photocatalytic and photoelectrochemical measurements

The photocatalytic toluene oxidation was carried out in a sealed 40 mL Pyrex bottle filled with 2.5 mg catalyst and 5 mL toluene. The whole system was degassed for two times to remove air and refilled with high-purity (99.999%) O₂. A 150 W Xe lamp (Zolix) coupled with an AM 1.5 G filter and a 420 nm cut-off filter was used as the light source (150 mW cm⁻²). After irradiating for 4 h, the reaction solution was filtered using organic filter head to remove the solid powders, then the filtrate was analyzed by gas chromatography (GC9790 plus, Fuli Analytical Instrument Co., Ltd.) equipped with a chromatographic column (Kromat Corporation, KB-FFAP 30 m × 0.32 mm × 1.00 μm). The photocatalytic recycle experiments were carried out under the same condition, with the reaction system being revacuumized and then refilled with O₂ for every 4 h. Four cycles were done. The control photocatalytic experiments in dark, without O₂ or catalyst, or with different radical scavengers have been conducted. Typically, *t*-butanol (50 μL), benzoquinone (BQ, 50 mg), ammonium oxalate (AO, 50 mg) and K₂S₂O₈ (50 mg) was utilized as the •OH, h⁺, •O₂⁻ and e⁻ scavenger, respectively. Transient photocurrent responses were carried out in a standard three-electrode setup connected to a CHI660E electrochemical workstation. The sample films prepared by centrifugation were used as the working electrode, and Pt plate and Ag/AgCl (saturated KCl) was used as the counter electrode and the reference electrode, respectively, and 0.25 mM tetrabutylammonium hexafluoro phosphate/isopropanol solution was used as the electrolyte. The same light source (150 mW cm⁻²) as the photocatalytic experiments was used, and the light on/off was controlled by a light chopping equipment (PFS40A, Beijing Perfect Light Technology Co., Ltd.).

2.6. Computational calculation

The CASTEP package implemented in Materials Studio was employed to perform the density functional theory (DFT) calculations [42], and the electronic exchange and correlation effects of materials were investigated through the generalized gradient approximation (GGA) with the Perdew-Burke-Ernzerhof (PBE) formulation [43–45]. The geometric optimization in the Brillouin zone was conducted by the uniform G-centered k-points meshes with a resolution of 2π × 0.04 Å⁻¹ and Methfessel-Paxton electronic smearing. The corresponding simulation was carried out based on the ultrasoft potential, and the cutoff energy was 500 eV. Above these settings ensured that the total energies for per atom were lower than 10⁻³ eV. All forces on atoms were smaller than 10⁻³ eV Å⁻¹ and the total stress tensor was smaller than 10⁻² GPa of the target value by the structure relaxation.

3. Results and discussion

3.1. The synthesis and characterization of samples

In view of self-templated precursor for growth Cs₃Bi₂Br₉, semiconductor Bi₂O₂CO₃ might be a promising choice because it can release Bi³⁺ during acid etching. However, Bi₂O₂CO₃ suffers a lot from the wide indirect bandgap (3.2–3.5 eV) with poor visible-light absorption [46]. Element doping or alloying is believed as an effective way to regulate the electronic band structure of semiconductor [47,48]. Herein, Co-doped Bi₂O₂CO₃ (denoted as Co_xBi_{2-x}O₂CO₃) was designed and synthesized via simple liquid phase deposition process (Fig. S1), in which the Co³⁺ content can be regulated easily by changing the Co:Bi feeding ratio. After the introduction of Co³⁺, the original white Bi₂O₂CO₃ powders changed to brown (Fig. S2a–d). Moreover, no extra XRD diffraction peaks as compared to Bi₂O₂CO₃ appeared, but the diffraction peaks gradually shifted toward higher angle with increasing the Co³⁺ content, as shown in Fig. S2e, f. The subtle structure changes should be attributed to the smaller radius of Co³⁺ than Bi³⁺, implying the successful introduction of Co³⁺ into the lattice of Bi₂O₂CO₃. The morphology characterization (Fig. S3) revealed that the interconnected nanosheet architecture of Bi₂O₂CO₃ can be reserved, but both the lateral size and thickness were reduced largely. Moreover, TEM analysis showed that the surface of the Co_xBi_{2-x}O₂CO₃ nanosheet was smooth with the lattice spacing of 0.275 and 0.688 nm being distinguished, which were assigned to the (110) and (002) planes of Co_xBi_{2-x}O₂CO₃. This slightly changed lattice than that of Bi₂O₂CO₃ further proved the successful introduction of Co³⁺ (Fig. S4). In addition, element analysis by ICP-AES (Table S1) revealed that the Co³⁺ content increased obviously with increasing the Co:Bi feeding ratio, e.g., the actual atom ratio of Co: Bi in Co_xBi_{2-x}O₂CO₃ (1:1) sample was 0.94:1, quite close to the initial feeding ratio. Thus, the Co_xBi_{2-x}O₂CO₃ sample discussed below was Co_xBi_{2-x}O₂CO₃ (1:1), which was denoted as the Co_{0.97}Bi_{1.03}O₂CO₃.

As mentioned above, the color of Bi₂O₂CO₃ turned from white to brown after the introduction of Co³⁺, indicating that the visible-light responsive ability had been changed. This conclusion could be testified by the UV–vis diffuse reflectance spectra of samples (Fig. S5), which showed a remarkable red shift from ~400 nm for Bi₂O₂CO₃ to ~810 nm for Co_{0.97}Bi_{1.03}O₂CO₃, corresponding to a dramatically reduced bandgap from 3.11 to 1.53 eV. This is an indicative of electronic band structure changes caused by Co³⁺. Thus, it is highly desired to understand the effect of Co³⁺ on the crystal structure and the corresponding electronic structure. To this end, the crystal structure of Co_{0.97}Bi_{1.03}O₂CO₃ was first determined by the Pawley refinement of its PXRD patterns. As shown in Fig. 1a and Table S2, the refinement results reveal that the unit-cell parameters (I2/m, a = 3.860 Å, b = 3.858 Å, c = 13.737 Å) of Co_{0.97}Bi_{1.03}O₂CO₃ change slightly comparing with those of Bi₂O₂CO₃ (I2/m, a = 3.865 Å, b = 3.862 Å, c = 13.675 Å), with the a- and b-axis slightly contracted while the c-axis slightly elongated. It could be speculated that the Bi³⁺ sites in Bi₂O₂CO₃ were replaced by Co³⁺ forming a solid solution-like structure, which was consistent with previous reports [48].

To further understand the Co³⁺-induced changes in the atomic/electronic structures and chemical environment, the X-ray absorption spectroscopy (XAS) analysis was applied to determine the structure of Co_{0.97}Bi_{1.03}O₂CO₃. Fig. 1b compares the Co K-edge X-ray absorption near edge structure (XANES) of Co_{0.97}Bi_{1.03}O₂CO₃ with some standard cobalt oxides or carbonates, which shows a slight shift to higher energy than the others. Given the fact the Co K-edge absorption mainly originates from the electron transition from Co 1 s core level to Co 4p unoccupied orbitals, it indicates the Co element of Co_{0.97}Bi_{1.03}O₂CO₃ behaves different oxidation states, d-electron occupancies and local atomic environments from those of reference materials. Compared with Co foil and CoO, the absorption edge of Co_{0.97}Bi_{1.03}O₂CO₃ is closer to that of Co₂O₃ and Co₃O₄, suggesting that it may exist as trivalent Co. Moreover, the Bi LIII-edge absorption (Fig. 1e) of Co_{0.97}Bi_{1.03}O₂CO₃ is

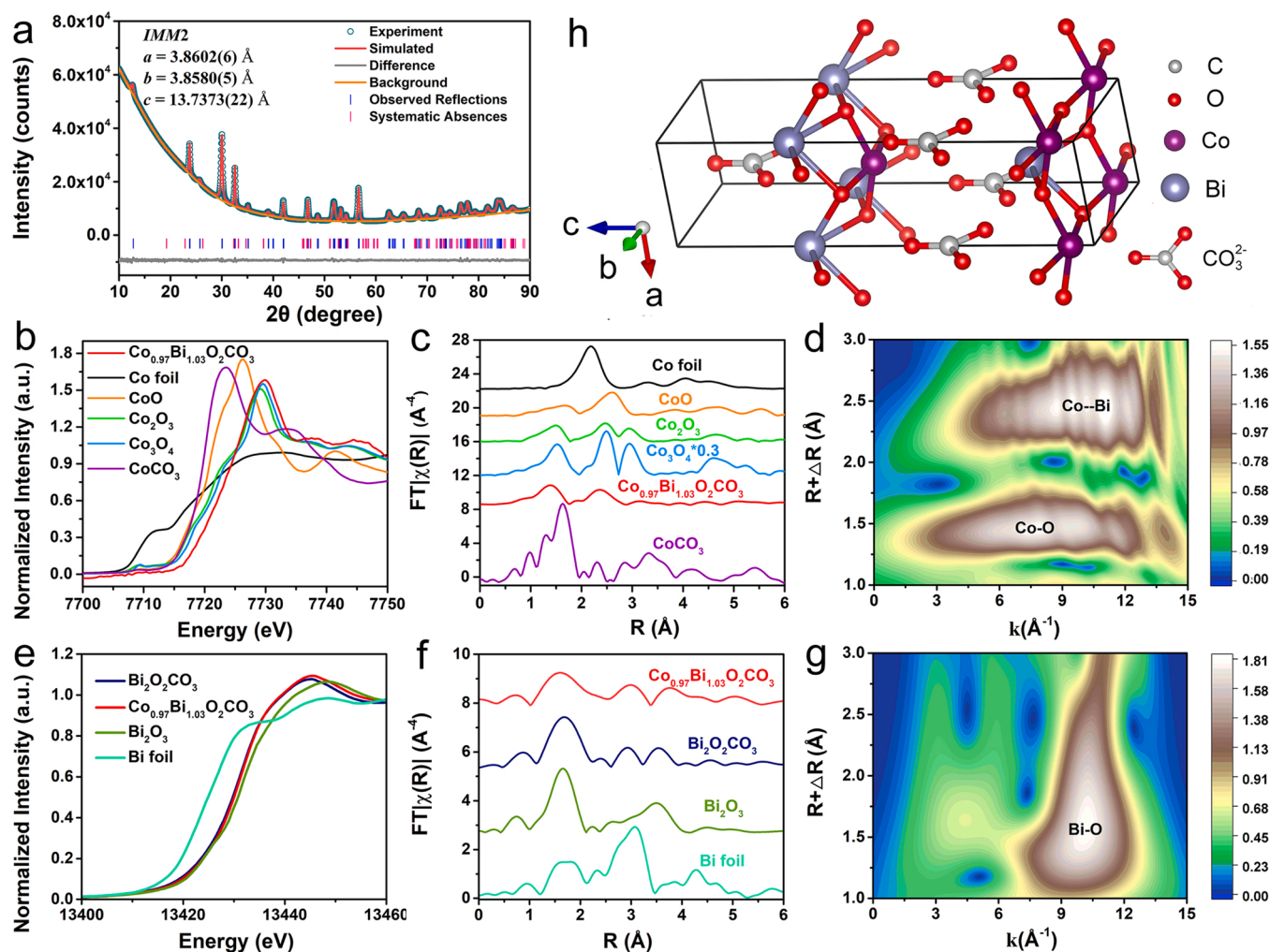


Fig. 1. The crystal structure and chemical environment for $\text{Co}_{0.97}\text{Bi}_{1.03}\text{O}_2\text{CO}_3$ sample. (a) The PXRD Pawley refinement pattern of $\text{Co}_{0.97}\text{Bi}_{1.03}\text{O}_2\text{CO}_3$, (b, e) Co K-edge and Bi LIII-edge XANES spectra, respectively, and (c, f) the corresponding Fourier transforms R space fitting results. (d, g) Wavelet transforms for k2-weighted EXAFS signals of Co and Bi element for $\text{Co}_{0.97}\text{Bi}_{1.03}\text{O}_2\text{CO}_3$, respectively. (h) The unit-cell structure of $\text{Co}_x\text{Bi}_{2-x}\text{O}_2\text{CO}_3$ with the theoretical atom ratio of 1:1 of Co: Bi.

almost the same as that of $\text{Bi}_2\text{O}_2\text{CO}_3$ and both of them are quite close to that of reference Bi_2O_3 sample, indicating the chemical valence of Bi element in the $\text{Co}_x\text{Bi}_{2-x}\text{O}_2\text{CO}_3$ is trivalent under the introduction of Co^{3+} . To further figure out the detailed structural parameters around Co^{3+} and Bi^{3+} in $\text{Co}_{0.97}\text{Bi}_{1.03}\text{O}_2\text{CO}_3$, the extended X-ray absorption fine structure (EXAFS) spectra and Fourier transform analysis were performed (Fig. 1c, f) and the corresponding fitting results were shown in Fig. S6, Table S3 and S4. For the $\text{Co}_{0.97}\text{Bi}_{1.03}\text{O}_2\text{CO}_3$, the average bond length ($R(\text{\AA})$) of Co-O is 1.89 \AA and the coordination number (CN) is 4.3 in the first shell. The $R(\text{\AA})$ value of Bi-O bond and CN is 2.24 \AA and 3.95, respectively, which is very similar to those of the pristine $\text{Bi}_2\text{O}_2\text{CO}_3$ ($R(\text{\AA}) = 2.23$ \AA and CN = 3.96, respectively). The corresponding wavelet transforms of $\text{Co}_{0.97}\text{Bi}_{1.03}\text{O}_2\text{CO}_3$ (Fig. 1d, g) show similar Co-O signals to those of cobalt oxides (Fig. S7), further confirming the formation of Co-O bonds. While the abscissa of Bi-O signals related to the strongest signal intensity region increases significantly comparing with that of $\text{Bi}_2\text{O}_2\text{CO}_3$ and Bi_2O_3 , which may be attributed to the Bi^{3+} replacement by a large number of Co^{3+} . These results signify that the introduction of Co^{3+} doesn't change the electronic environment of Bi^{3+} obviously; moreover, there are four O in the nearest shell of Co^{3+} and four Bi^{3+} in its second shell. The Co^{3+} has replaced the position of Bi^{3+} forming a pyramid-like structure. Therefore, the structure model of $\text{Co}_{0.97}\text{Bi}_{1.03}\text{O}_2\text{CO}_3$ can be built (Fig. 1h), in which the lattice constants are $a = 3.577$ \AA , $b = 4.110$ \AA , and $c = 13.719$ \AA , respectively (Table S2). This unit-cell

difference can be attributed to the different tested depths of the PXRD Pawley refinement and EXAFS methods. However, due to the smaller electronegativity of Bi (1.02) than that of Co (1.88), the CO_3^{2-} group between layers would migrate from the original equilibrium state to Co-terminated metal-O layer leading to the increased O numbers in the first shell coordination environment of Co and decreased electron density, which should account for the positive shift of Co K-edge absorption in $\text{Co}_{0.97}\text{Bi}_{1.03}\text{O}_2\text{CO}_3$ (Fig. 1b).

To further shed light on the crystal structure and photoelectrical properties of $\text{Co}_{0.97}\text{Bi}_{1.03}\text{O}_2\text{CO}_3$, DFT calculation was carried out based on the foregoing PXRD refinement results. As shown in Fig. S8, the optimized crystal structure shows that part of Bi^{3+} are replaced by Co^{3+} and the whole cell volume is reduced by only 1.18% as compared to original $\text{Bi}_2\text{O}_2\text{CO}_3$, which is in accordance with the XRD refinement and XAS results (Table S2). In addition, the calculated bond lengths of Co-O, Bi-O and Co-Bi are close to the XAS results with the D-value of only 0.02 \AA . Furthermore, the calculated projected density of states (PDOS) analysis (Fig. 2a, b) reveals that the valence band maximum (VBM) of $\text{Bi}_2\text{O}_2\text{CO}_3$ is mainly dictated by the O 2p orbital, but it changes to the cooperation of O 2p and Co 3d orbitals for $\text{Co}_{0.97}\text{Bi}_{1.03}\text{O}_2\text{CO}_3$. While the conduction band minimum (CBM) of $\text{Bi}_2\text{O}_2\text{CO}_3$ consists of Bi 6p and O 2p orbitals, it also changes to O 2p and Co 3d orbitals for $\text{Co}_{0.97}\text{Bi}_{1.03}\text{O}_2\text{CO}_3$. Therefore, the band structure transforms from wide indirect bandgap (3.11 eV) for $\text{Bi}_2\text{O}_2\text{CO}_3$ to narrow direct bandgap

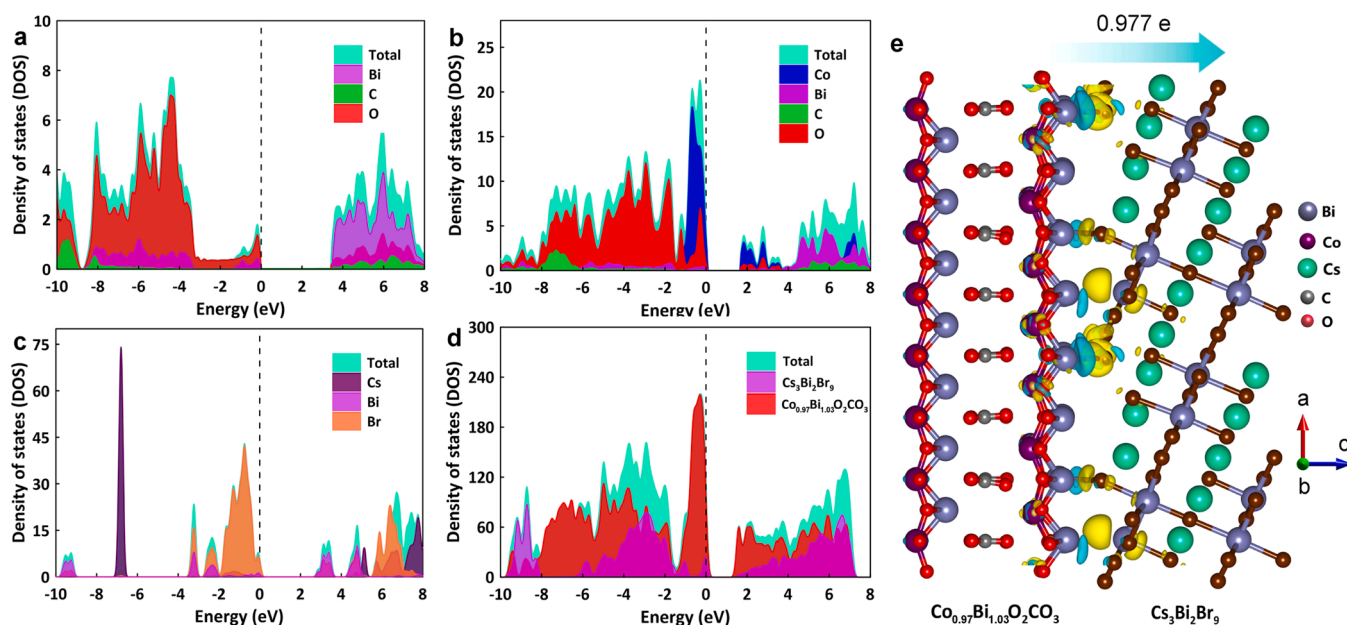


Fig. 2. Theoretical characterization of the energy band structures and electronic properties of samples. The calculated total and projected density of states of (a) $\text{Bi}_2\text{O}_2\text{CO}_3$, (b) $\text{Co}_{0.97}\text{Bi}_{1.03}\text{O}_2\text{CO}_3$, (c) $\text{Cs}_3\text{Bi}_2\text{Br}_9$ and (d) $\text{Co}_{0.97}\text{Bi}_{1.03}\text{O}_2\text{CO}_3/\text{Cs}_3\text{Bi}_2\text{Br}_9$ heterojunction. (e) The calculated charge density difference (CDD) of the heterojunction, the yellow and blue area represents the electron accumulation and depletion, respectively.

(1.53 eV) for $\text{Co}_{0.97}\text{Bi}_{1.03}\text{O}_2\text{CO}_3$ (Fig. S9), agreeing well with the experimental values. The above results indicate the successful synthesis of bimetallic $\text{Co}_x\text{Bi}_{2-x}\text{O}_2\text{CO}_3$ nanosheets, and the introduction of Co^{3+} can maintain the original laminar structure of $\text{Bi}_2\text{O}_2\text{CO}_3$ and regulate the electronic structure, leading to the formation of new direct bandgap semiconductor with high visible-light harvesting ability.

3.2. In situ growth of $\text{Co}_x\text{Bi}_{2-x}\text{O}_2\text{CO}_3/\text{Cs}_3\text{Bi}_2\text{Br}_9$ heterojunction

The as-prepared $\text{Co}_{0.97}\text{Bi}_{1.03}\text{O}_2\text{CO}_3$ nanosheets were used as the self-template for Bi^{3+} to *in situ* grow $\text{Co}_{0.97}\text{Bi}_{1.03}\text{O}_2\text{CO}_3/\text{Cs}_3\text{Bi}_2\text{Br}_9$ heterojunction via Bi bridge (Fig. 3a). After the reaction, characteristic diffraction peaks of hexagonal $\text{Cs}_3\text{Bi}_2\text{Br}_9$ appear and the products change from dark brown to brownish yellow (Fig. S10). Moreover, TEM images reveal that the ridge-like tiny nanosheets with thickness of ~ 2 nm emerge on the originally smooth surface of $\text{Co}_{0.97}\text{Bi}_{1.03}\text{O}_2\text{CO}_3$ nanosheets (Fig. 3b). The lattice spacing of ridge-like structure is 0.310 nm, corresponding to the (112) plane of $\text{Cs}_3\text{Bi}_2\text{Br}_9$, and the lattice spacing of the background nanosheet is 0.275 nm, which could be assigned to the (110) plane of $\text{Co}_{0.97}\text{Bi}_{1.03}\text{O}_2\text{CO}_3$ (Fig. 3c). The HAADF-STEM image also confirms this fascinating tiny nanosheets grown on nanosheet architecture, and the line scan element analysis finds that more Bi elements exist in ridge-like region (Fig. S11). In addition, the corresponding EDX element mapping (Fig. 1e-j) demonstrates the homogeneous distribution of targeted C, O, Bi, Co, Cs and Br elements in the hybrid nanosheets. It should be noted that the $\text{Co}_{0.97}\text{Bi}_{1.03}\text{O}_2\text{CO}_3$ precursor could be completely transformed into $\text{Cs}_3\text{Bi}_2\text{Br}_9$ if excess HBr solution was added, with yellow curved nanosheets can be obtained (Fig. S10 and S12).

All these results corroborated the successful construction of $\text{Co}_{0.97}\text{Bi}_{1.03}\text{O}_2\text{CO}_3/\text{Cs}_3\text{Bi}_2\text{Br}_9$ heterojunction via self-templated acid etching procedure. The fascinating nanosheet grown on nanosheet architecture therewith inspires us to explore the underlying growth mechanism of heterojunction. Detailed crystal structure analysis shows that both $\text{Co}_{0.97}\text{Bi}_{1.03}\text{O}_2\text{CO}_3$ and $\text{Cs}_3\text{Bi}_2\text{Br}_9$ exhibit lamellar structure. However, interlayer insertion growth and face to face growth are not preferential choice owing to the high lattice mismatch ($f=27.19\%$) of Bi-Bi distance between the orthorhombic $\text{Co}_{0.97}\text{Bi}_{1.03}\text{O}_2\text{CO}_3$ (100) facet and hexagonal $\text{Cs}_3\text{Bi}_2\text{Br}_9$ (100) facet, and the different crystal plane

angle (Fig. S13). It is found that the Bi-Bi distance in (112) face of $\text{Cs}_3\text{Bi}_2\text{Br}_9$ is 14.200 Å, which matches well with the distance between five Bi atoms in (002) face of $\text{Co}_{0.97}\text{Bi}_{1.03}\text{O}_2\text{CO}_3$ with small f of 0.75% (Fig. 3d). Therefore, it can be speculated that the anchor of (112) of $\text{Cs}_3\text{Bi}_2\text{Br}_9$ on (002) of $\text{Co}_x\text{Bi}_{2-x}\text{O}_2\text{CO}_3$ might be allowable. In this case, $\text{Cs}_3\text{Bi}_2\text{Br}_9$ can epitaxially grow along (001) face forming an angle of 51.06° with the layer of $\text{Co}_{0.97}\text{Bi}_{1.03}\text{O}_2\text{CO}_3$, which might account for the upright growth of $\text{Cs}_3\text{Bi}_2\text{Br}_9$ nanosheets on the surface of $\text{Co}_{0.97}\text{Bi}_{1.03}\text{O}_2\text{CO}_3$ nanosheets.

Interestingly, only irregular $\text{Cs}_3\text{Bi}_2\text{Br}_9$ particles can be obtained when $\text{Bi}_2\text{O}_2\text{CO}_3$ nanosheet was used as the self-template instead (Fig. S14). This result implied that, in addition to the crystal lattice factor, the integration of Co^{3+} in the crystal lattice should also play significant role in the controlled growth of 2D/2D heterojunction. According to the structure analysis of $\text{Co}_{0.97}\text{Bi}_{1.03}\text{O}_2\text{CO}_3$, the Co-O bond length is shorter than Bi-O bond, indicating that Bi-O bond is more likely to be etched when HBr is added. Some previous reports also illustrated that CoO_x materials always exhibited stronger tolerance to acid than BiO_x materials [49,50]. Therefore, the Co-O layer interspersed between Bi-O layer can slow down the acid etching speed of $\text{Co}_{0.97}\text{Bi}_{1.03}\text{O}_2\text{CO}_3$ to control the release of Bi^{3+} , in the meantime, maintain the structure integrity of parent nanosheet. The supposed heterojunction growth process is illustrated in Fig. 3a, due to the buffer effect of Co-O layer, part of Bi-O bands on the surface of $\text{Co}_{0.97}\text{Bi}_{1.03}\text{O}_2\text{CO}_3$ nanosheets are destroyed to sustained release Bi^{3+} when HBr is added, and the morphology of mother nanosheets can be retained. The released Bi^{3+} can react with Cs^+ and Br^- in precursor solution to produce $\text{Cs}_3\text{Bi}_2\text{Br}_9$ and the surface Bi atoms may serve as anchor points to induce the nucleation and growth. These effect of Co, in combine with the matched Bi lattice between $\text{Co}_{0.97}\text{Bi}_{1.03}\text{O}_2\text{CO}_3$ with $\text{Cs}_3\text{Bi}_2\text{Br}_9$, thus trigger the epitaxial growth of $\text{Cs}_3\text{Bi}_2\text{Br}_9$ nanosheet to produce ridge-like 2D/2D heterostructure. To verify the effect of Co-O layer, some similar Bi-based nanosheets, including $\text{Co}_x\text{Bi}_{2-x}\text{O}_2(\text{OH})_2$, $\text{Co}_x\text{Bi}_{2-x}\text{O}_2\text{Br}_2$, $\text{Fe}_x\text{Bi}_{2-x}\text{O}_2\text{CO}_3$ and $\text{Ni}_x\text{Bi}_{2-x}\text{O}_2\text{CO}_3$, were also synthesized for the *in situ* growth of $\text{Cs}_3\text{Bi}_2\text{Br}_9$. As expected, ridge-like heterojunctions were obtained when Co-containing $\text{Co}_x\text{Bi}_{2-x}\text{O}_2(\text{OH})_2$ or $\text{Co}_x\text{Bi}_{2-x}\text{O}_2\text{Br}_2$ were used as the self-template, whereas only quantum dot-on-nanosheet structure was achieved by using the $\text{Fe}_x\text{Bi}_{2-x}\text{O}_2\text{CO}_3$ or $\text{Ni}_x\text{Bi}_{2-x}\text{O}_2\text{CO}_3$ as the template (Fig. S15). This result confirmed the pivotal role of Co-O layer, but also

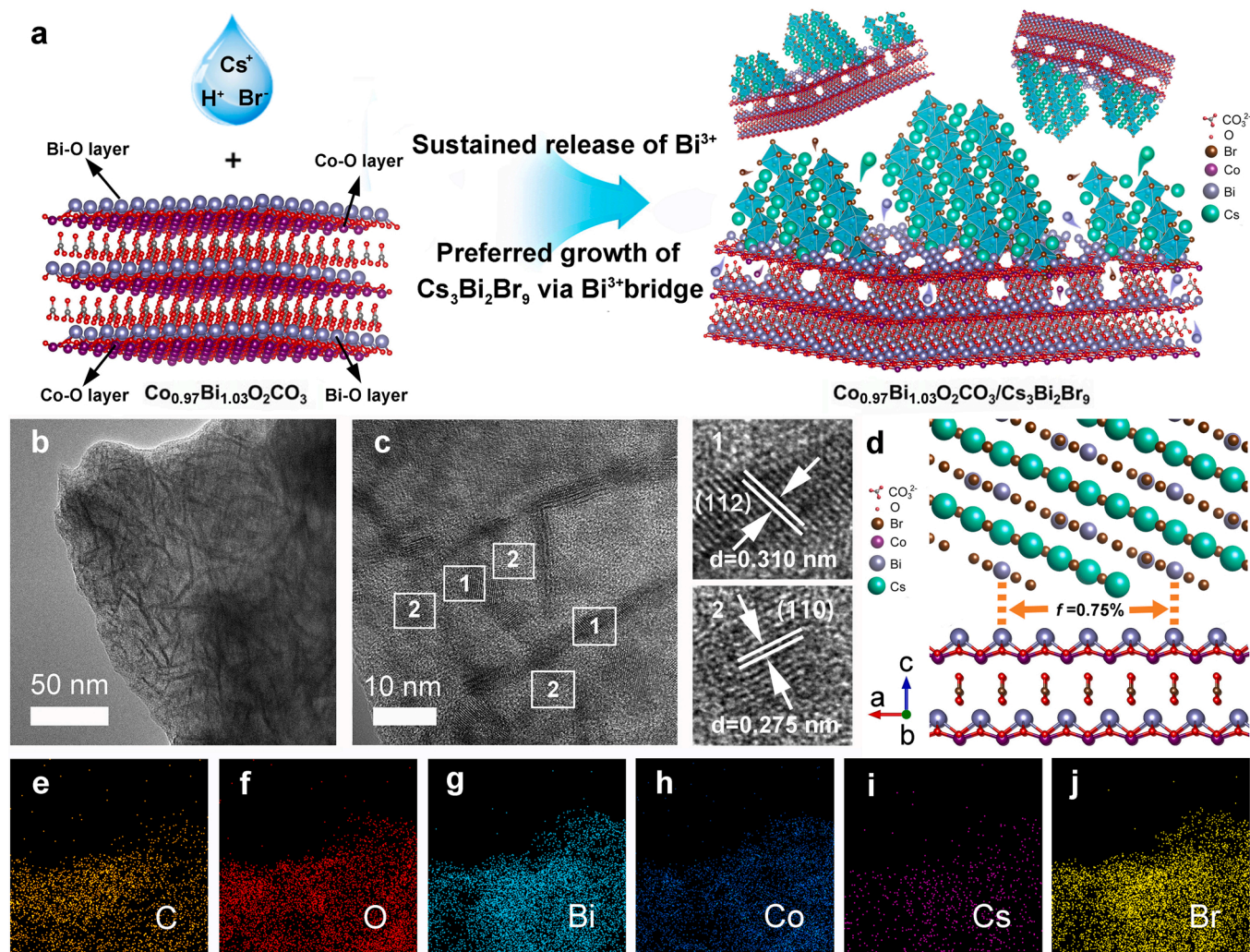


Fig. 3. Formation mechanism and structural investigation for the heterojunction. (a) The formation schematic diagram of $\text{Co}_{0.97}\text{Bi}_{1.03}\text{O}_2\text{CO}_3/\text{Cs}_3\text{Bi}_2\text{Br}_9$ heterojunction, (b) TEM, (c) HRTEM image and (d) the lattice match of $\text{Co}_{0.97}\text{Bi}_{1.03}\text{O}_2\text{CO}_3/\text{Cs}_3\text{Bi}_2\text{Br}_9$ hybrid; (e–j) the corresponding energy dispersive X-ray (EDX) elemental mapping images.

implied the proposed acid etching self-template procedure was universal to construct *in situ* heterojunction. In addition, the control experiments by adjusting the dropping speed and addition volume of HBr-containing precursor solution also found that the growth speed of $\text{Cs}_3\text{Bi}_2\text{Br}_9$ was quite fast and the numbers of the $\text{Cs}_3\text{Bi}_2\text{Br}_9$ nanosheets increased with increasing the amount of precursor solution, which meant that the amount of heterointerfaces was adjustable (Fig. S16).

3.3. Characterization of photoelectric properties and charge transfer

Fig. 4a displays the normalized UV–vis diffuse reflectance spectra of as-prepared heterojunction. Compared with parent $\text{Co}_{0.97}\text{Bi}_{1.03}\text{O}_2\text{CO}_3$, the formation of $\text{Cs}_3\text{Bi}_2\text{Br}_9$ induces a strong absorption before ~ 480 nm ($E_g = 2.58$ eV), which is consistent with the absorption of thoroughly converted $\text{Cs}_3\text{Bi}_2\text{Br}_9$ sample [12,16]. This result indicates the hybrid integrates the light absorption properties of the $\text{Co}_{0.97}\text{Bi}_{1.03}\text{O}_2\text{CO}_3$ and $\text{Cs}_3\text{Bi}_2\text{Br}_9$. To figure out the photo-induced charge transfer properties, the band configuration of heterojunction was therewith analyzed. As revealed by UPS measurement (Fig. 4b), the work function (W_F) of $\text{Co}_{0.97}\text{Bi}_{1.03}\text{O}_2\text{CO}_3$ and $\text{Cs}_3\text{Bi}_2\text{Br}_9$ is 4.40 and 4.52 eV (vs. vacuum), respectively. Combining with the bandgap values, the CBM (E_{CB}) and the VBM (E_{VB}) of $\text{Co}_{0.97}\text{Bi}_{1.03}\text{O}_2\text{CO}_3$ is calculated to be -0.64 and 0.89 V vs. normal hydrogen electrode (NHE), respectively, and the E_{CB} and E_{VB} value of $\text{Cs}_3\text{Bi}_2\text{Br}_9$ is -0.38 and 2.20 V vs. NHE, respectively. Thus,

staggered band structure is formed with the Fermi level of $\text{Co}_{0.97}\text{Bi}_{1.03}\text{O}_2\text{CO}_3$ higher than that of $\text{Cs}_3\text{Bi}_2\text{Br}_9$ (Fig. S17a). Therefore, Fermi levels alignment would happen when the two components got close contact with each other, the charge redistribution of which would result in the band bending and the formation of interfacial built-in electric field (IEF) pointing from $\text{Co}_{0.97}\text{Bi}_{1.03}\text{O}_2\text{CO}_3$ to $\text{Cs}_3\text{Bi}_2\text{Br}_9$ (Fig. S17b). This charge transfer ability was first confirmed by DFT differential charge density analysis. According to PDOS analysis (Fig. 2b–d), the VBM of $\text{Co}_{0.97}\text{Bi}_{1.03}\text{O}_2\text{CO}_3$ in the hybrid is higher than that of $\text{Cs}_3\text{Bi}_2\text{Br}_9$, whereas the CBM of $\text{Co}_{0.97}\text{Bi}_{1.03}\text{O}_2\text{CO}_3$ and $\text{Cs}_3\text{Bi}_2\text{Br}_9$ are overlap. As a consequence, the preferable charge redistribution might be occurred at the interfaces. As depicted in Fig. 2e, obvious electrons transfer from $\text{Co}_{0.97}\text{Bi}_{1.03}\text{O}_2\text{CO}_3$ to $\text{Cs}_3\text{Bi}_2\text{Br}_9$ can be observed at the heterointerface, and the Bader charge is as high as 0.977 e, reflecting the strong interfacial electronic coupling interaction that may contribute to large IEF.

Generally, the intensity of IEF largely depend on the quality of heterointerface, strong enough IEF can guide the photo-generated charge carriers transporting via Z-scheme route. Otherwise, type II heterojunction would form [51–54]. To figure out the interface interaction and charge transfer mechanism of $\text{Co}_{0.97}\text{Bi}_{1.03}\text{O}_2\text{CO}_3/\text{Cs}_3\text{Bi}_2\text{Br}_9$ 2D/2D heterojunction, the XPS measurements in dark and under irradiation were performed (Fig. 4c–h and Fig. S18). When measured in dark, the Co 2p signal of heterojunction exhibits two peaks at 780.59 and 795.62 eV,

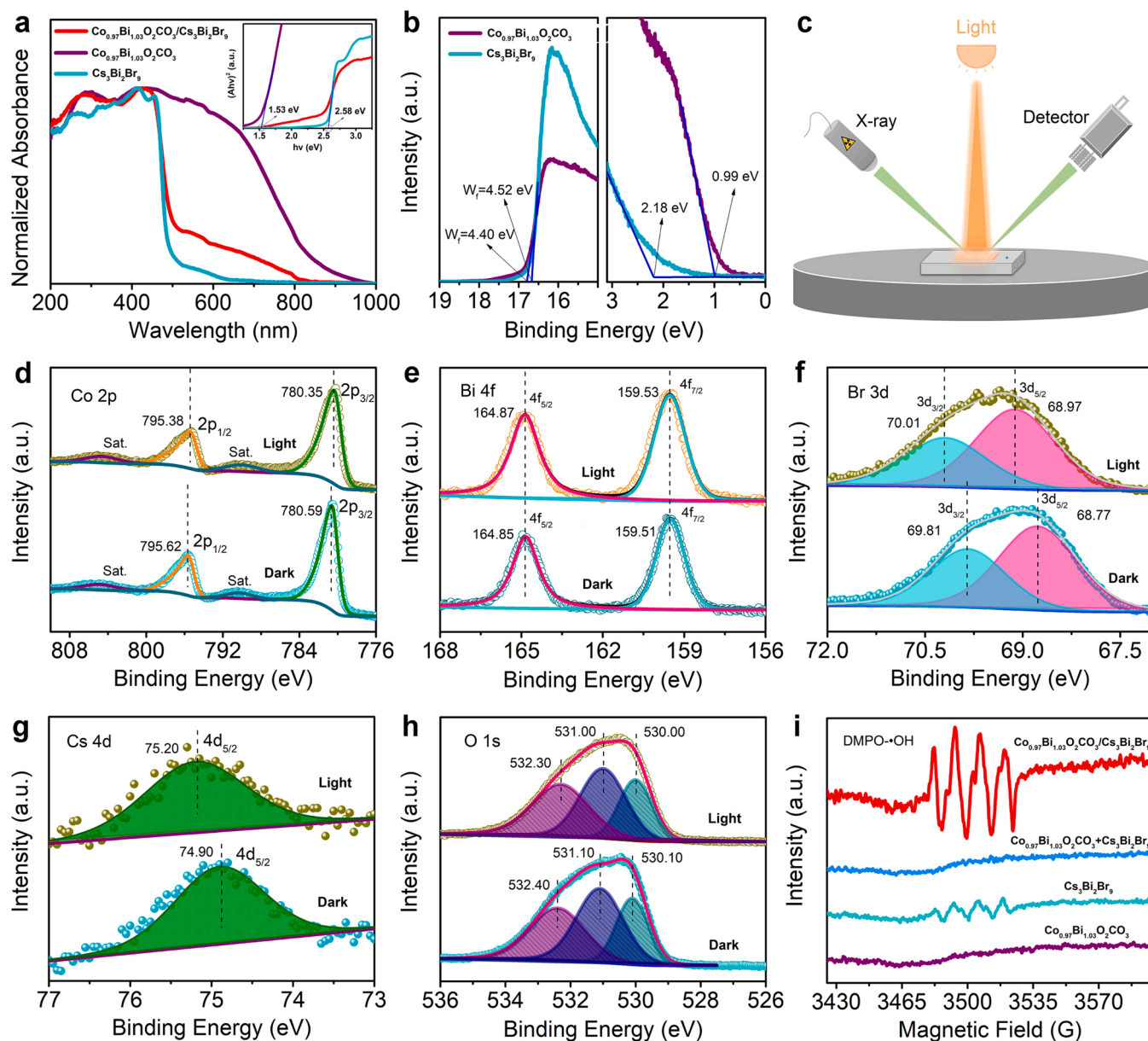


Fig. 4. Photophysical properties and photogenerated charge carriers transfer investigation. (a) Normalized UV-vis absorption spectra and Tauc plots of the samples. (b) UPS of $\text{Co}_{0.97}\text{Bi}_{1.03}\text{O}_2\text{CO}_3$ and $\text{Cs}_3\text{Bi}_2\text{Br}_9$. (c) Schematic illustration of the *in situ* XPS test in dark and under illumination and (d-h) the corresponding XPS spectra of $\text{Co}_{0.97}\text{Bi}_{1.03}\text{O}_2\text{CO}_3/\text{Cs}_3\text{Bi}_2\text{Br}_9$ heterojunction: d) Co 2p; e) Bi 4f; f) Br 3d; g) Cs 4d, and h) O 1s i) EPR spectra of DMPO-•OH adduct under the irradiation of visible light for 5 min.

respectively, accompanied by two shake-up satellite peaks, which can be assigned to the binding energies (BEs) of Co $2p_{3/2}$ and Co $2p_{1/2}$. The O 1s spectra reveal the presence of lattice oxygen (530.10 eV), carbonate species (531.1 eV) and adsorbed H_2O or surface -OH (532.4 eV). The Bi 4f signal shows two peaks at 159.51 and 164.85 eV, respectively, corresponding to Bi $4f_{7/2}$ and Bi $4f_{5/2}$. Noticeably, the binding energies of Co 2p and O 1s in the $\text{Co}_{0.97}\text{Bi}_{1.03}\text{O}_2\text{CO}_3/\text{Cs}_3\text{Bi}_2\text{Br}_9$ heterojunction shift toward higher values by 0.42 and 0.37 eV, respectively, in comparison with those of parent $\text{Co}_{0.97}\text{Bi}_{1.03}\text{O}_2\text{CO}_3$, while the Br 3d signal exhibits a negative shift (by ~ 0.37 eV) relative to that of bare $\text{Cs}_3\text{Bi}_2\text{Br}_9$. These results indicate the formation of strong chemical and electronic coupling interaction at the heterointerfaces, which can provide effective electron transfer pathways from $\text{Co}_{0.97}\text{Bi}_{1.03}\text{O}_2\text{CO}_3$ to $\text{Cs}_3\text{Bi}_2\text{Br}_9$ during the Fermi levels alignment. On the contrast, when illuminated at 405 nm, it was found that the binding energies of Co 2p and O 1s in heterojunction shifted negatively by 0.24 and 0.1 eV, respectively, implying an

increased electron density of Co and O under illumination (Fig. 4d, e). Whereas the Cs 4d and Br 3d signals exhibit a positive shift by 0.30 and 0.20 eV, respectively, suggesting a decrease in electron density (Fig. 4f, g). This opposite BEs shift direction before and after illumination proves that the photoexcited electrons in $\text{Cs}_3\text{Bi}_2\text{Br}_9$ transfer to $\text{Co}_{0.97}\text{Bi}_{1.03}\text{O}_2\text{CO}_3$ under light irradiation, following a Z-scheme pathway. On the contrast, the same binding energy shift direction of Co 2p, O 1s, and Br 3d before and after illumination are observed for the physically mixed $\text{Co}_{0.97}\text{Bi}_{1.03}\text{O}_2\text{CO}_3 + \text{Cs}_3\text{Bi}_2\text{Br}_9$ sample (Fig. S18), indicating the photoexcited charge carriers transferred in a type-II transfer mechanism, which should be attributed to the weak interaction between $\text{Co}_{0.97}\text{Bi}_{1.03}\text{O}_2\text{CO}_3$ and $\text{Cs}_3\text{Bi}_2\text{Br}_9$ nanosheets. Therefore, it can be concluded that the strong chemical and electronic coupling interaction at the *in situ* growth heterointerfaces should account for a strong IEF, which can drive the Z-scheme transport of charge. The formation of Z-scheme heterojunction can be proved further by EPR tests

using DMPO to capture $\cdot\text{OH}$ species. According to the band position (Fig. S17), both the CBM of $\text{Co}_{0.97}\text{Bi}_{1.03}\text{O}_2\text{CO}_3$ and $\text{Cs}_3\text{Bi}_2\text{Br}_9$ can drive the production of $\cdot\text{O}_2^-$, but the VBM of $\text{Co}_{0.97}\text{Bi}_{1.03}\text{O}_2\text{CO}_3$ is too negative to participate the production of $\cdot\text{OH}$ species. If type-II heterojunction was formed, no DMPO- $\cdot\text{OH}$ signals should be detected since photoinduced holes would accumulate on the VBM of $\text{Co}_{0.97}\text{Bi}_{1.03}\text{O}_2\text{CO}_3$. However, obvious DMPO- $\cdot\text{OH}$ signals with relative intensities of 1:2:2:1 can be clearly observed for the $\text{Co}_{0.97}\text{Bi}_{1.03}\text{O}_2\text{CO}_3/\text{Cs}_3\text{Bi}_2\text{Br}_9$ (Fig. 4i), indicating a Z-scheme electron transfer happened in the heterojunction. That is, the photoinduced electrons at CBM of $\text{Cs}_3\text{Bi}_2\text{Br}_9$ would recombine with the holes in the VBM of $\text{Co}_{0.97}\text{Bi}_{1.03}\text{O}_2\text{CO}_3$, leaving photoinduced electrons and holes with higher redox ability on the CBM of $\text{Co}_{0.97}\text{Bi}_{1.03}\text{O}_2\text{CO}_3$ and VBM of $\text{Cs}_3\text{Bi}_2\text{Br}_9$, respectively. By contrast, the physically mixed $\text{Co}_{0.97}\text{Bi}_{1.03}\text{O}_2\text{CO}_3 + \text{Cs}_3\text{Bi}_2\text{Br}_9$ sample exhibited no DMPO- $\cdot\text{OH}$ signals, confirming that a type-II charge transfer pathway formed among the simple physical mixing sample, as depicted in Fig. S17.

Then the charge transfer and separation ability of such 2D/2D $\text{Co}_{0.97}\text{Bi}_{1.03}\text{O}_2\text{CO}_3/\text{Cs}_3\text{Bi}_2\text{Br}_9$ heterojunction was examined. Fig. S19 shows the transient photocurrent responses of samples. Under chopped light, $\text{Co}_{0.97}\text{Bi}_{1.03}\text{O}_2\text{CO}_3$ nanosheet film exhibits very weak response current. Whereas the $\text{Co}_{0.97}\text{Bi}_{1.03}\text{O}_2\text{CO}_3/\text{Cs}_3\text{Bi}_2\text{Br}_9$ heterojunction produces a photocurrent of $\sim 4.45 \mu\text{A cm}^{-2}$, which is approximately 2 times than that of pristine $\text{Cs}_3\text{Bi}_2\text{Br}_9$ ($\sim 2.22 \mu\text{A cm}^{-2}$), and about 4 times larger than that of the physically mixed $\text{Co}_{0.97}\text{Bi}_{1.03}\text{O}_2\text{CO}_3 + \text{Cs}_3\text{Bi}_2\text{Br}_9$ ($\sim 1.08 \mu\text{A cm}^{-2}$). It implies that the *in situ* growth of $\text{Co}_{0.97}\text{Bi}_{1.03}\text{O}_2\text{CO}_3/\text{Cs}_3\text{Bi}_2\text{Br}_9$ heterojunction can effectively promote the photogenerated charge transfer and separation. Moreover, the KPFM tests of samples (Fig. 5) reveal that distinctive surface photovoltage (SPV) changes up to +45.18 mV can be observed in the $\text{Co}_{0.97}\text{Bi}_{1.03}\text{O}_2\text{CO}_3/\text{Cs}_3\text{Bi}_2\text{Br}_9$ heterojunction film before and after illumination, much higher than that of pristine $\text{Co}_{0.97}\text{Bi}_{1.03}\text{O}_2\text{CO}_3$ film where almost no SPV changes can be observed, suggesting a more effective charge separation and transfer in the heterojunction. Since the surface of heterojunction was mainly covered by $\text{Cs}_3\text{Bi}_2\text{Br}_9$ nanosheets, the positive SPV signals upon

illumination indicated that the photoexcited holes should accumulated on $\text{Cs}_3\text{Bi}_2\text{Br}_9$ nanosheets, further confirming the Z-scheme charge transfer process and the resulted spacial separation of photoexcited charge carriers.

3.4. Photocatalytic performance measurements and charge transfer mechanism of heterojunctions

In view of the aforementioned results, a high-quality direct Z-scheme $\text{Co}_{0.97}\text{Bi}_{1.03}\text{O}_2\text{CO}_3/\text{Cs}_3\text{Bi}_2\text{Br}_9$ heterojunction was fabricated successfully. To further check the charge separation efficiency, the photocatalytic toluene oxidation reaction under visible-light irradiation was carried out. This reaction was selected due to the VBM of $\text{Co}_{0.97}\text{Bi}_{1.03}\text{O}_2\text{CO}_3$ is not positive enough to drive the photooxidation of toluene to form benzyl radicals. Only if a Z-scheme heterojunction was formed, the heterojunction could drive the catalytic reaction of toluene (Fig. 6a-b). As illustrated in Fig. 6c, the pristine $\text{Co}_{0.97}\text{Bi}_{1.03}\text{O}_2\text{CO}_3$ exhibits no catalytic activity for toluene oxidation due to its mismatched CBM. By contrast, the $\text{Cs}_3\text{Bi}_2\text{Br}_9$ behaves relatively good photocatalytic activity with a conversion rate of $882.74 \mu\text{mol g}^{-1} \text{h}^{-1}$ for benzaldehyde. As expected, the $\text{Co}_{0.97}\text{Bi}_{1.03}\text{O}_2\text{CO}_3/\text{Cs}_3\text{Bi}_2\text{Br}_9$ heterojunction exhibits the best catalytic activity with a benzaldehyde yield rate of $1837.31 \mu\text{mol g}^{-1} \text{h}^{-1}$, 2.08 times higher than that of bare $\text{Cs}_3\text{Bi}_2\text{Br}_9$. The selectivity for benzaldehyde can reach 90.10%. In stark contrast, no photocatalytic activity can be observed for the physically mixed $\text{Co}_{0.97}\text{Bi}_{1.03}\text{O}_2\text{CO}_3 + \text{Cs}_3\text{Bi}_2\text{Br}_9$ since type-II charge transfer formed in this sample, where the content of $\text{Cs}_3\text{Bi}_2\text{Br}_9$ was low and hence most of them might contact with $\text{Co}_{0.97}\text{Bi}_{1.03}\text{O}_2\text{CO}_3$ nanosheets. In this case, the holes (h^+) of $\text{Co}_{0.97}\text{Bi}_{1.03}\text{O}_2\text{CO}_3$ nanosheets would move to the VB of $\text{Co}_{0.97}\text{Bi}_{1.03}\text{O}_2\text{CO}_3$, where the photoinduced h^+ accumulated on the VB of $\text{Co}_{0.97}\text{Bi}_{1.03}\text{O}_2\text{CO}_3$ cannot drive the toluene oxidation reaction. These results further confirmed the conclusion that high-quality interfaces with atomic-level close-contact and strong chemical interaction are formed in such *in situ* $\text{Co}_{0.97}\text{Bi}_{1.03}\text{O}_2\text{CO}_3/\text{Cs}_3\text{Bi}_2\text{Br}_9$ heterojunction, which contributes to a strong built-in electric field at the interfaces to

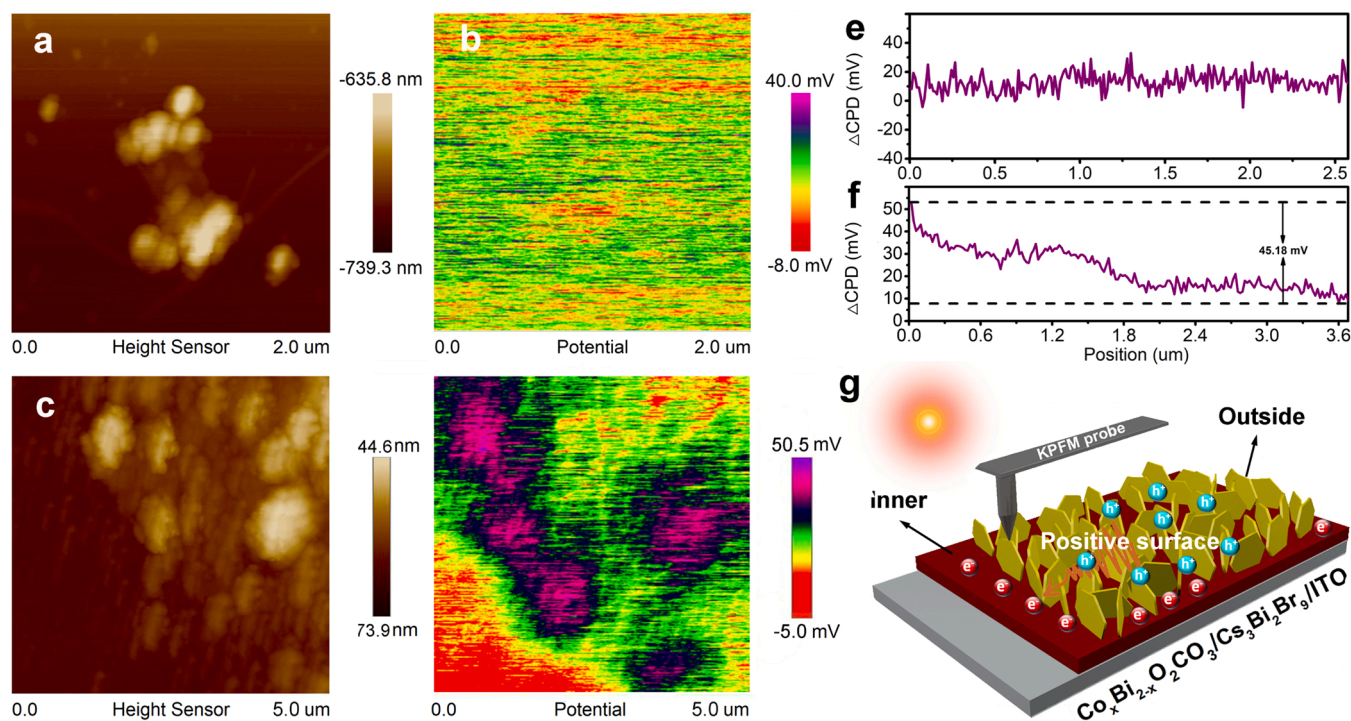


Fig. 5. The surface photovoltage (SPV) measurements. KPFM measurement of $\text{Co}_{0.97}\text{Bi}_{1.03}\text{O}_2\text{CO}_3$ and $\text{Co}_{0.97}\text{Bi}_{1.03}\text{O}_2\text{CO}_3/\text{Cs}_3\text{Bi}_2\text{Br}_9$ samples. (a, c) AFM height images; (b, d) the surface photovoltage (SPV) difference ($\Delta\text{CPD} = \text{CPD}_{\text{light}} - \text{CPD}_{\text{dark}}$) images and (e, f) represent corresponding line profiles of the SPV difference. (g) schematic diagram of the accumulation of photoinduced electrons and holes among the heterojunction.

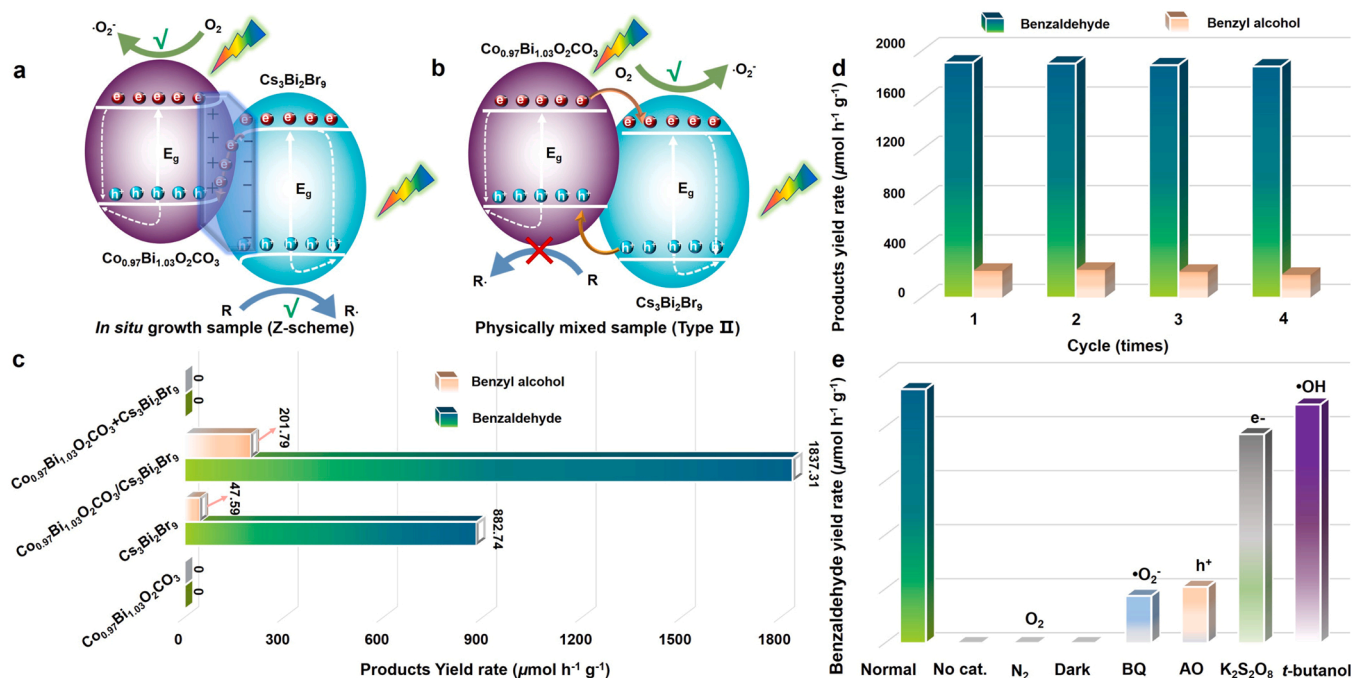


Fig. 6. The charge transfer mechanism and photocatalytic performance test of heterojunction. The photogenerated carriers transfer process of (a) *in situ*-grown Co_{0.97}Bi_{1.03}O₂CO₃/Cs₃Bi₂Br₉ heterojunction and (b) physically mixed Co_{0.97}Bi_{1.03}O₂CO₃ + Cs₃Bi₂Br₉ sample. (c) Comparison of the photocatalytic toluene oxidation performances of different samples under AM 1.5 G, 150 mW cm⁻². (d) Cycling photocatalytic toluene oxidation performance of the Co_{0.97}Bi_{1.03}O₂CO₃/Cs₃Bi₂Br₉ hybrid of 4 cycles (4 h for each cycle) under visible-light illumination. (e) Control photocatalytic experiments of the Co_{0.97}Bi_{1.03}O₂CO₃/Cs₃Bi₂Br₉ hybrid heterojunction under different reaction conditions.

drive the fast Z-scheme transportation and spacial separation of photo-excited charge carriers. The unique advantages of such Co_{0.97}Bi_{1.03}O₂CO₃/Cs₃Bi₂Br₉ heterojunction also suggests that the well-designed structure is quite favorable for the consecutive charge transfer and separation. Additionally, the cycling stability of the hybrid heterojunction was also evaluated. As shown in Fig. 6d, no obvious degradations of product yields were observed after 4 consecutive cycles. Furthermore, no significant phase structure changes emerged in the XRD pattern of sample after cycling reaction, confirming the good photocatalytic stability of Co_{0.97}Bi_{1.03}O₂CO₃/Cs₃Bi₂Br₉ heterojunction. To figure out the active species of the photocatalytic process, the control experiments have also been carried out in dark, without O₂ or catalyst, or with different radical scavengers, as summarized in Fig. 6e. Neither benzaldehyde nor benzyl alcohol was produced in N₂ atmosphere, without catalyst or illumination, indicating that the O₂, catalyst and light source were the three prerequisites for driving the toluene oxidation reaction. Moreover, the formation rate of benzaldehyde was largely inhibited when the ammonium oxalate (AO) and benzoquinone (BQ) was added as the h⁺ scavenger and •O₂ scavenger, respectively. Whereas, slight performance decay was found with the introduction of *t*-butanol and K₂S₂O₈ as the •OH and e⁻ scavenger, respectively. Therefore, it can be concluded that h⁺ and •O₂ intermediates were the key species in utilizing the solar energy to convert toluene into high value-added oxygenated products.

4. Conclusions

In conclusion, we have successfully constructed a novel *in situ* Co_xBi_{2-x}O₂CO₃/Cs₃Bi₂Br₉ 2D/2D heterojunction *via* self-templated acid etching process. It is revealed that the matched Bi lattice and the sustained release of Bi³⁺ by Co³⁺-doping in Bi₂O₂CO₃ are of vital importance in enabling epitaxial growth of Cs₃Bi₂Br₉ nanosheets on Co_xBi_{2-x}O₂CO₃ nanosheets. Moreover, the incorporation of Co³⁺ can regulate the electron structure to form staggered band structure with Cs₃Bi₂Br₉. As a result, the atomic-level close-contact heterointerfaces

with strong chemical and electronic coupling can be built *via* cosharing Bi atom. A strong built-in electric field was found at the Co_{0.97}Bi_{1.03}O₂CO₃/Cs₃Bi₂Br₉ interfaces, which resulted in a fast Z-scheme charge transfer, and thus enabled significantly enhanced toluene photo-oxidation performances when compared with the Cs₃Bi₂Br₉. This work unveils an effective “atom-triggered” strategy to design high-quality lead-free heterojunctions *via* composition and interface manipulation, which may be expected to broaden the horizons of developing other advanced photocatalytic materials.

CRediT authorship contribution statement

Yuan Teng: Experimental, Conceptualization, Methodology, Formal analysis, Data curation, Validation, Resources, Funding acquisition, Writing – original draft, Writing – review & editing. **Jing-Hua Chen:** Experimental, Conceptualization, Methodology, Formal analysis, Data curation, Validation, Resources, Writing – review & editing. **Yu-Hua Huang:** Experimental, Conceptualization, Validation. **Zi-Chun Zhou:** Experimental, Resources, Formal analysis. **Xu-Dong Wang:** Supervision, Writing – original draft, Resources. **Dai-Bin Kuang:** Supervision, Project administration, Funding acquisition, Writing – original draft, Writing – review & editing. **Hong-Yan Chen:** Conceptualization, Supervision, Project administration, Funding acquisition, Writing – original draft, Writing – review & editing.

Declaration of Competing Interest

The authors declare that they have no known competing financial interests or personal relationships that could have appeared to influence the work reported in this paper.

Data Availability

Data will be made available on request.

Acknowledgments

The authors acknowledge the financial supports received from the National Natural Science Foundation of China (22175202, 22005351, 21875288), the LIRT Project of Guangdong PRTP (2017BT01C161), the Guangdong Basic and Applied Basic Research Foundation (2019A15110513, 2020A15110937, 2023A1515010180) and the Program of Guangzhou Science and Technology (202201011591). The authors would like to thank Z.M.Y. for his assistance in the PXRD refinement and structural analysis.

Appendix A. Supporting information

Supplementary data associated with this article can be found in the online version at [doi:10.1016/j.apcatb.2023.122889](https://doi.org/10.1016/j.apcatb.2023.122889).

References

- [1] C.R. Roy, D.X. Pan, Y.N. Wang, M.P. Hautzinger, Y.Z. Zhao, J.C. Wright, Z.H. Zhu, S. Jin, Anion exchange of ruddlesden-popper lead halide perovskites produces stable lateral heterostructures, *J. Am. Chem. Soc.* 143 (2021) 5212–5221.
- [2] K.O. Brinkmann, T. Becker, F. Zimmermann, C. Kreusel, T. Gahlmann, M. Theisen, T. Haeger, S. Olthof, C. Tückmantel, M. Günster, T. Maschwitz, F. Göbelsmann, C. Koch, D. Hertel, P. Caprioglio, F. Peña-Camargo, L. Perdigón-Toro, A. Al-Ashouri, L. Merten, A. Hinderhofer, L. Gomell, S. Zhang, F. Schreiber, S. Albrecht, K. Meerholz, D. Neher, M. Stollerfoht, T. Riedl, Perovskite-organic tandem solar cells with indium oxide interconnect, *Nature* 604 (2022) 280–286.
- [3] S. Park, W.J. Chang, C.W. Lee, S. Park, H.-Y. Ahn, K.T. Nam, Photocatalytic hydrogen generation from hydriodic acid using methylammonium lead iodide in dynamic equilibrium with aqueous solution, *Nat. Energy* 2 (2017) 16185.
- [4] C.-C. Lin, T.-R. Liu, S.-R. Lin, K.M. Boopathi, C.-H. Chiang, W.-Y. Tzeng, W.-H. C. Chien, H.-S. Hsu, C.-W. Luo, H.-Y. Tsai, H.-A. Chen, P.-C. Kuo, J. Shiue, J.-W. Chiou, W.-F. Pong, C.-C. Chen, C.-W. Chen, Spin-polarized photocatalytic CO₂ reduction of Mn-doped perovskite nanoplates, *J. Am. Chem. Soc.* 144 (2022) 15718–15726.
- [5] T.C. Jellicoe, J.M. Richter, H.F.J. Glass, M. Tabachnyk, R. Brady, S.E. Dutton, A. Rao, R.H. Friend, D. Credgington, N.C. Greenham, M.L. Böhm, Synthesis and optical properties of lead-free cesium tin halide perovskite nanocrystals, *J. Am. Chem. Soc.* 138 (2016) 2941–2944.
- [6] S.S. Bhosale, A.K. Kharade, E. Jorak, A. Fathi, S. Chang, E.W.-G. Diau, Mechanism of photocatalytic CO₂ reduction by bismuth-based perovskite nanocrystals at the gas-solid interface, *J. Am. Chem. Soc.* 141 (2019) 20434–20442.
- [7] Y.T. Dai, C. Poidevin, C. Ochoa-Hernández, A.A. Auer, H. Tüysüz, A supported bismuth halide perovskite photocatalyst for selective aliphatic and aromatic C-H bond activation, *Angew. Chem. Int. Ed.* 59 (2020) 5788–5796.
- [8] J.C. Pi, X.F. Jia, Z.W. Long, S. Yang, H. Wu, D.C. Zhou, Q. Wang, H.B. Zheng, Y. Yang, J.Y. Zhang, J.B. Qiu, Surface and defect engineering coupling of halide double perovskite Cs₂NaBiCl₆ for efficient CO₂ photoreduction, *Adv. Energy Mater.* 12 (2022), 2202074.
- [9] Z.Z. Zhang, Y.Y. Yang, Y.Y. Wang, L.L. Yang, Q. Li, L.X. Chen, D.S. Xu, Revealing the A-site effect of lead-free A₃Sb₂Br₉ perovskite in photocatalytic C(sp³)-H bond activation, *Angew. Chem. Int. Ed.* 59 (2020) 18136–18139.
- [10] G.Q. Chen, P. Wang, Y.Q. Wu, Q.Q. Zhang, Q. Wu, Z.Y. Wang, Z.K. Zheng, Y.Y. Liu, Y. Dai, B.B. Huang, Lead-free halide perovskite Cs₃Bi₂Sb₂xI₉ (x ≈ 0.3) possessing the photocatalytic activity for hydrogen evolution comparable to that of (CH₃NH₃)PbI₃, *Adv. Mater.* 32 (2020), 2001344.
- [11] P.F. Cheng, L. Sun, L. Feng, S.Q. Yang, Y. Yang, D.Y. Zheng, Y. Zhao, Y.B. Sang, R. L. Zhang, D.H. Wei, W.Q. Deng, K.L. Han, Colloidal synthesis and optical properties of all-inorganic low-dimensional cesium copper halide nanocrystals, *Angew. Chem. Int. Ed.* 58 (2019) 16087–16091.
- [12] B. Yang, J.S. Chen, F. Hong, X. Mao, K.B. Zheng, S.Q. Yang, Y.J. Li, T. Pullerits, W. Q. Deng, K.L. Han, Lead-free, air-stable all-inorganic cesium bismuth halide perovskite nanocrystals, *Angew. Chem. Int. Ed.* 56 (2017) 12471–12475.
- [13] Q.Q. Fan, G.V. Biesold-McGee, J.Z. Ma, Q.N. Xu, S. Pan, J. Peng, Z.Q. Lin, Lead-free halide perovskite nanocrystals: crystal structures, synthesis, stabilities, and optical properties, *Angew. Chem. Int. Ed.* 59 (2020) 1030–1046.
- [14] L. Lu, X. Pan, J.H. Luo, Z.H. Sun, Recent advances and optoelectronic applications of lead-free halide double perovskites, *Chem. Eur. J.* 26 (2020) 16975–16984.
- [15] Y.F. Xu, M.Z. Yang, B.X. Chen, X.D. Wang, H.Y. Chen, D.B. Kuang, C.Y. Su, A CsPbBr₃ perovskite quantum dot/graphene oxide composite for photocatalytic CO₂ reduction, *J. Am. Chem. Soc.* 139 (2017) 5660–5663.
- [16] L. Romani, A. Speltini, C.N. Dibenedetto, A. Listorti, F. Ambrosio, E. Mosconi, A. Simbula, M. Saba, A. Profumo, P. Quadrelli, F. De Angelis, L. Malavasi, Experimental strategy and mechanistic view to boost the photocatalytic activity of Cs₃Bi₂Br₉ lead-free perovskite derivative by g-C₃N₄ composite engineering, *Adv. Funct. Mater.* 31 (2021), 2104428.
- [17] Q.-M. Sun, J.-J. Xu, F.-F. Tao, W. Ye, C. Zhou, J.-H. He, J.-M. Lu, Boosted inner surface charge transfer in perovskite nanodots/mesoporous titania framework for efficient CO₂ photoreduction to methane, *Angew. Chem. Int. Ed.* 61 (2022), e202200.
- [18] X.L. Zhao, S. Chen, H.J. Yin, S.Y. Jiang, K. Zhao, J. Kang, P.F. Liu, L.X. Jiang, Z. J. Zhu, D.D. Cui, P.R. Liu, X.J. Han, H.G. Yang, H.J. Zhao, Perovskite microcrystals with intercalated monolayer MoS₂ nanosheets as advanced photocatalyst for solar-powered hydrogen generation, *Matter* 3 (2020) 935–949.
- [19] L.-Y. Wu, Y.-F. Mu, X.-X. Guo, W. Zhang, Z.-M. Zhang, M. Zhang, T.-B. Lu, Encapsulating perovskite quantum dots in iron-based metal-organic frameworks (MOFs) for efficient photocatalytic CO₂ reduction, *Angew. Chem. Int. Ed.* 58 (2019) 9491–9495.
- [20] P. Zhou, H. Chen, Y.G. Chao, Q.H. Zhang, W.Y. Zhang, F. Lv, L. Gu, Q. Zhao, N. Wang, J.S. Wang, S.J. Guo, Single-atom Pt-I₃ sites on all-inorganic Cs₂SnI₆ perovskite for efficient photocatalytic hydrogen production, *Nat. Commun.* 12 (2021) 4412.
- [21] Y. Jiang, H.-Y. Chen, J.-Y. Li, J.-F. Liao, H.-H. Zhang, X.-D. Wang, D.-B. Kuang, Z-scheme 2D/2D heterojunction of CsPbBr₃/Bi₂WO₆ for improved photocatalytic CO₂ reduction, *Adv. Funct. Mater.* 30 (2020), 2004293.
- [22] M. Ou, W.G. Tu, S.M. Yin, W.N. Xing, S.Y. Wu, H.J. Wang, S.P. Wan, Q. Zhong, R. Xu, Amino-assisted anchoring of CsPbBr₃ perovskite quantum dots on porous g-C₃N₄ for enhanced photocatalytic CO₂ reduction, *Angew. Chem. Int. Ed.* 57 (2018) 13570–13574.
- [23] S.K. Balakrishnan, P.V. Kamat, Au-CsPbBr₃ hybrid architecture: anchoring gold nanoparticles on cubic perovskite nanocrystals, *ACS Energy Lett.* 2 (2017) 88–93.
- [24] Z.-J. Li, E. Hofman, J. Li, A.H. Davis, C.-H. Tung, L.-Z. Wu, W.W. Zheng, Photoelectrochemically active and environmentally stable CsPbBr₃/TiO₂ core/shell nanocrystals, *Adv. Funct. Mater.* 28 (2018), 1704288.
- [25] X.C. Jiao, X.D. Li, X.Y. Jin, Y.F. Sun, J.Q. Xu, L. Liang, H.X. Ju, J.F. Zhu, Y. Pan, W. S. Yan, Y. Lin, Y. Xie, Partially oxidized SnS₂ atomic layers achieving efficient visible-light-driven CO₂ reduction, *J. Am. Chem. Soc.* 139 (2017) 18044–18051.
- [26] S. Wang, B.Y. Guan, X.W.D. Lou, Construction of ZnIn₂S₄-In₂O₃ hierarchical tubular heterostructures for efficient CO₂ photoreduction, *J. Am. Chem. Soc.* 140 (2018) 5037–5040.
- [27] Y.Q. Tang, C.H. Mak, R.G. Liu, Z.K. Wang, L. Ji, H.S. Song, C.Y. Tan, F. Barrière, H.-Y. Hsu, In situ formation of bismuth-based perovskite heterostructures for high-performance cocatalyst-free photocatalytic hydrogen evolution, *Adv. Funct. Mater.* 30 (2020), 2006919.
- [28] Z.-L. Liu, R.-R. Liu, Y.-F. Mu, Y.-X. Feng, G.-X. Dong, M. Zhang, T.-B. Lu, In situ construction of lead-free perovskite direct Z-scheme heterojunction Cs₃Bi₂I₉/Bi₂WO₆ for efficient photocatalysis of CO₂ reduction, *Sol. RRL* 5 (2021), 2000691.
- [29] J.Y. Li, H.Y. Chen, Y. Jiang, D.-B. Kuang, In situ construction of direct Z-scheme Cs_xWO₃/CsPbBr₃ heterojunctions via cosharing Cs Atom, *Sol. RRL* 5 (2021), 2100036.
- [30] J. Chen, D.J. Morrow, Y. Fu, W. Zheng, Y. Zhao, L. Dang, M.J. Stolt, D.D. Kohler, X. Wang, K.J. Czech, M.P. Hautzinger, S. Shen, L. Guo, A. Pan, J.C. Wright, S. Jin, Single-crystal thin films of cesium lead bromide perovskite epitaxially grown on metal oxide perovskite (SrTiO₃), *J. Am. Chem. Soc.* 139 (2017) 13525–13532.
- [31] W.M. Tian, J. Leng, C.Y. Zhao, S.Y. Jin, Long-distance charge carrier funneling in perovskite nanowires enabled by built-in halide gradient, *J. Am. Chem. Soc.* 139 (2017) 579–582.
- [32] M.-Y. Kuo, N. Spitha, M.P. Hautzinger, P.-L. Hsieh, J. Li, D.X. Pan, Y.Z. Zhao, L.-J. Chen, M.H. Huang, S. Jin, Y.-J. Hsu, J.C. Wright, Distinct carrier transport properties across horizontally vs vertically oriented heterostructures of 2D/3D perovskites, *J. Am. Chem. Soc.* 143 (2021) 4969–4978.
- [33] C. Jia, H. Li, X.W. Meng, H.B. Li, CsPbX₃/Cs₄PbX₆ core/shell perovskite nanocrystals, *Chem. Comm.* 54 (2018) 6300–6303.
- [34] Z.J. Ning, X.W. Gong, R. Comin, F. Fan, O. Voznyy, E. Yassitepe, A. Buin, S. Hoogland, E.H. Sargent, Quantum-dot-in-perovskite solids, *Nature* 523 (2015) 324–328.
- [35] M.X. Liu, Y.L. Chen, C.-S. Tan, R. Quintero-Bermudez, A.H. Proppe, R. Munir, H. R. Tan, O. Voznyy, B. Scheffe, G. Walters, A.P.T. Kam, B. Sun, M.-J. Choi, S. Hoogland, A. Amassian, S.O. Kelle, F.P. García de Arquer, E.H. Sargent, Lattice anchoring stabilizes solution-processed semiconductors, *Nature* 570 (2019) 96–101.
- [36] B. Yang, W.C. Pan, H.D. Wu, G.D. Niu, J.-H. Yuan, K.-H. Xue, L.X. Yin, X.Y. Du, X.-S. Miao, X.Q. Yang, Q.G. Xie, J. Tang, Heteroepitaxial passivation of Cs₂AgBiBr₆ wafers with suppressed ionic migration for X-ray imaging, *Nat. Commun.* 10 (2019) 1989.
- [37] X. Zhang, X. Wu, X. Liu, G. Chen, Y. Wang, J. Bao, X. Xu, X. Liu, Q. Zhang, K. Yu, W. Wei, J. Liu, J. Xu, H. Jiang, P. Wang, X. Wang, Heterostructural CsPbX₃-PbS (X = Cl, Br, I) quantum dots with tunable vis-NIR dual emission, *J. Am. Chem. Soc.* 142 (2020) 4464–4471.
- [38] J.B. Zhang, X.F. Liu, P.F. Jiang, H.T. Chen, Y. Wang, J.M. Ma, R. Zhang, F. Yang, M. K. Wang, J. Zhang, G.L. Tu, Red-emitting CsPbBr₃/PbSe heterojunction nanocrystals with high luminescent efficiency and stability for bright light-emitting diodes, *Nano Energy* 66 (2019), 104142.
- [39] M. Imran, L.C. Peng, A. Pianetti, V. Pinchetti, J. Ramade, J. Zito, F.D. Stasio, J. Buba, S. Toso, J. Song, I. Infante, S. Bals, S. Brovelli, L. Manna, Halide perovskite-lead chalcogenide nanocrystal heterostructures, *J. Am. Chem. Soc.* 143 (2021) 1435–1446.
- [40] X.Y. Zhang, T.T. Zhu, C.M. Ji, Y.P. Yao, J.H. Luo, In situ epitaxial growth of centimeter-sized lead-free (BA)₂CsAgBiBr₇/Cs₂AgBiBr₆ heterocrystals for self-driven X-ray detection, *J. Am. Chem. Soc.* 143 (2021) 20802–20810.
- [41] X.-D. Wang, Y.-H. Huang, J.-F. Liao, Y. Jiang, L. Zhou, X.-Y. Zhang, H.-Y. Chen, D.-B. Kuang, In situ construction of a Cs₂SnI₆ perovskite nanocrystal/SnS₂ nanosheet heterojunction with boosted interfacial charge transfer, *J. Am. Chem. Soc.* 141 (2019) 13434–13441.

- [42] S.J. Clark, M.D. Segall, C.J. Pickard, P.J. Hasnip, M.J. Probert, K. Refson, M. C. Payne, First principles methods using CASTEP, *Z. Krist. Cryst. Mater.* 220 (2005) 567–570.
- [43] P.E. Blöchl, Projector augmented-wave method, *Phys. Rev. B* 50 (1994) 17953–17979.
- [44] J.P. Perdew, K. Burke, M. Ernzerhof, Generalized gradient approximation made simple, *Phys. Rev. Lett.* 77 (1996) 3865–3868.
- [45] G. Kresse, D. Joubert, From ultrasoft pseudopotentials to the projector augmented-wave method, *Phys. Rev. B* 59 (1999) 1758–1775.
- [46] L.S. Wang, H.S. Yin, S. Wang, J. Wang, S.Y. Ai, Ni^{2+} -assisted catalytic one-step synthesis of $\text{Bi}/\text{BiOCl}/\text{Bi}_2\text{O}_2\text{CO}_3$ heterojunction with enhanced photocatalytic activity under visible light, *Appl. Catal. B Environ.* 305 (2022), 121039.
- [47] D.-X. Zhao, G.-P. Lu, C. Cai, Efficient visible-light-driven Suzuki coupling reaction over Co-doped BiOCl/Ce -doped $\text{Bi}_2\text{O}_2\text{CO}_3$ composites, *Green. Chem.* 23 (2021) 1823–1833.
- [48] J. Olchowka, H. Kabbour, M. Colmont, M. Adlung, C. Wickleder, O. Mentré, ABiO_2X (A = Cd, Ca, Sr, Ba, Pb; X = halogen) Sillen X1 series: polymorphism versus optical properties, *Inorg. Chem.* 55 (2016) 7582–7592.
- [49] J.S. Mondschein, J.F. Callejas, C.G. Read, J.Y.C. Chen, C.F. Holder, C.K. Badding, R.E. Schaak, Crystalline cobalt oxide films for sustained electrocatalytic oxygen evolution under strongly acidic conditions, *Chem. Mater.* 29 (2017) 950–957.
- [50] Y. Wang, B.C. Zhu, B. Cheng, W. Macyk, P.Y. Kuang, J.G. Yu, Hollow carbon sphere-supported Pt/CoO_x hybrid with excellent hydrogen evolution activity and stability in acidic environment, *Appl. Catal. B Environ.* 314 (2022), 121503.
- [51] L.X. Wang, C.B. Bie, J.G. Yu, Challenges of Z-scheme photocatalytic mechanisms, *Trends Chem.* 4 (2022) 973–983.
- [52] X.H. Niu, X.W. Bai, Z.B. Zhou, J.L. Wang, Rational design and characterization of direct Z-scheme photocatalyst for overall water splitting from excited state dynamics simulations, *ACS Catal.* 10 (2020) 1976–1983.
- [53] W.W. Xu, W. Tian, L.X. Meng, F.R. Cao, L. Li, Interfacial chemical bond-modulated Z-scheme charge transfer for efficient photoelectrochemical water splitting, *Adv. Energy Mater.* 11 (2021), 2003500.
- [54] X. Li, C. Garlisi, Q.S. Guan, S. Anwer, K. Al-Ali, G. Palmisano, L.X. Zheng, A review of material aspects in developing direct Z-scheme photocatalysts, *Mater. Today* 47 (2021) 75–107.